Journal Pre-proof

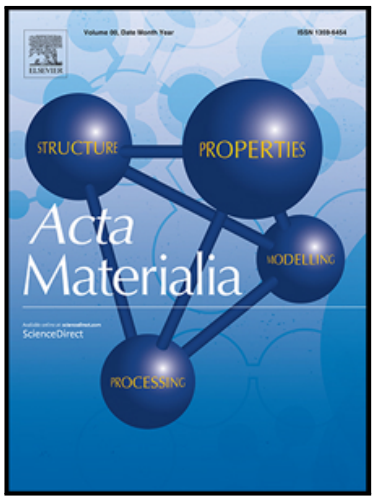

MX precipitate behavior in an irradiated advanced Fe-9Cr steel: Self-ion irradiation effects on phase stability

T.M. Kelsy Green , Tim Graening , Weicheng Zhong , Ying Yang , Kevin G. Field

PII: S1359-6454(25)00490-2
DOI: https://doi.org/10.1016/j.actamat.2025.121203
Reference: AM 121203

To appear in: *Acta Materialia*

Received date: 1 September 2024
Revised date: 31 May 2025
Accepted date: 1 June 2025

Please cite this article as: T.M. Kelsy Green , Tim Graening , Weicheng Zhong , Ying Yang , Kevin G. Field , MX precipitate behavior in an irradiated advanced Fe-9Cr steel: Self-ion irradiation effects on phase stability, *Acta Materialia* (2025), doi: https://doi.org/10.1016/j.actamat.2025.121203

This is a PDF file of an article that has undergone enhancements after acceptance, such as the addition of a cover page and metadata, and formatting for readability, but it is not yet the definitive version of record. This version will undergo additional copyediting, typesetting and review before it is published in its final form, but we are providing this version to give early visibility of the article. Please note that, during the production process, errors may be discovered which could affect the content, and all legal disclaimers that apply to the journal pertain.

© 2025 Published by Elsevier Inc. on behalf of Acta Materialia Inc.

Journal Pre-proof

MX precipitate behavior in an irradiated advanced Fe-9Cr steel: Self-ion irradiation effects on phase stability

T.M. Kelsy Green[a*], Tim Graening[b], Weicheng Zhong[b], Ying Yang[b], and Kevin G. Field[c]

[a]University of Michigan-Ann Arbor, currently at Antares Industries
[b]Oak Ridge National Laboratory
[c]University of Michigan-Ann Arbor

*Corresponding Author: kelsy@antaresindustries.com

Abstract

In an effort to optimize Fe-9Cr reduced activation ferritic/martensitic (RAFM) steels and to inform the design and operation of fusion reactors, this work represents the first in a series of cohesive studies dedicated to the evolution of MX-TiC precipitates under accelerated single and dual ion irradiations. This study investigates CNA9, a simplified Fe-9Cr RAFM steel featuring initial MX-TiC precipitate densities of $(2.3\pm0.3)\times10^{21}$ m^{-3}. This material was subjected to single self-ion irradiation at damage levels ranging from 1 to 100 displacements per atom (dpa) over a temperature range of 300 to 600°C, with a nominal dose rate of 7×10^{-4} dpa/s. Irradiation-induced coarsening was observed, as evidenced by statistically significant increases in mean diameter sizes, at 15 dpa at both 500°C and 600°C, whereas no coarsening was noted at 300°C or 400°C. Complete dissolution of precipitates occurred at damage levels of 50 and 100 dpa across the two temperatures tested (300°C and 500°C) while no significant changes were observed at any doses below 15 dpa at 500°C. Experimentally parameterized recoil resolution modeling suggests that the observed radiation stability of MX-TiC precipitates is intricately linked to diffusional changes of solutes resulting from the co-evolution of microstructural features within the experiments. The findings align with current theoretical perspectives on radiation-induced precipitate stability in complex alloys.

Journal Pre-proof

1.1 Introduction

Designing and manufacturing structural materials that can operate optimally in the harsh environment of a fusion reactor core for long life spans remains a hurdle for fusion energy deployment. Reduced activation ferritic/martensitic (RAFM) steels are the favored candidate structural materials for first-wall and blanket components in fusion reactors [1, 2] due to their inherent microstructural complexity, leading to resistance to radiation-induced degradation [3]. RAFM steels are body-centered cubic (BCC) Fe-based alloys with 7-15 weight % Cr and 1-3 weight % minor alloying solutes [4]. The inherent complexity of RAFM steels is derived from their grain structure, containing prior austenite grains, subgrains, and martensitic laths; their secondary phases, such as $M_{23}C_6$ and MX precipitates; and their high, pre-existing dislocation densities (~10^{14} m^{-2}) [5].

Of particular strategic importance for improving the high temperature creep strength [6] and increasing the sink strength of RAFM steels [7, 8] is the inclusion and stability of MX (M=metal, X=C and/or N) precipitates, found on and within grain boundaries. MX precipitates and $M_{23}C_6$ and MC-type precipitates have been studied in various FM and RAFM steels. For instance, studies have shown that MX precipitates in Eurofer97 steels tend to grow under neutron irradiation while maintaining similar number densities [9, 10]. Structure changes are also possible, an example being that $M_{23}C_6$ is known to undergo radiation-induced amorphization during in-situ TEM ion irradiations in additively manufactured Grade 91 and Eurofer97 [11]. In HT9 steels, VN precipitates are notably susceptible to radiation-enhanced segregation, leading to possible transformations into Cr-rich Z phases [12]. Different compositions of MX precipitates, such as VN, TaC, and NbC, exhibit varying stability under irradiation. Ta-rich precipitates such as TaC have generally shown better coarsening and dissolution resistance than other MX phases like VN

[13]. Radiation-induced changes in V-rich MX precipitates often shift toward increased Cr, Mo, Fe, and Si content post-irradiation, suggesting their composition adjusts continuously under irradiation [14].

Despite these insights, there is a notable lack of systematic documentation on the stability of MX precipitates, particularly MX-TiC precipitates, which are key target phases for advanced RAFM steels. This gap is especially pronounced for traditional ferritic/martensitic (FM) and advanced RAFM steels under conditions relevant to fusion environments, including those involving helium transmutation effects or their simulations [9, 10, 12-29]. MX-TiC precipitates have been extensively studied in Ti-modified austenitic steels, where their stability is governed by an interplay of concentration gradients, recoil resolution (ballistic dissolution), temperature, and steel processing before irradiation [30-40]. However, the extension or transferability of the current understanding of MX-TiC precipitate behavior in austenitic steels to FM or RAFM steels has not been well established. As the stability of these precipitates is crucial for maintaining creep and sink strength throughout the operation of a fusion reactor (>100 dpa) [27, 41-43], a comprehensive analysis of MX-TiC precipitate behavior is imperative. Furthermore, a nuanced understanding of MX-TiC precipitate behavior could provide valuable insights into the intricate relationship between precipitation and swelling in future research.

This work is the first in a series of three papers to systematically evaluate MX-TiC precipitate behavior in RAFM steels under various ion irradiation conditions, culminating in understanding MX-TiC precipitate stability and swelling in dual ion irradiations. This work will look at the precipitate stability under single-beam self-ion irradiation to isolate the effects of temperature and damage level on MX-TiC precipitate stability. A combination of ion irradiation

Journal Pre-proof

experiments, with careful post-irradiation characterization techniques coupled with an experimentally parameterized precipitate stability model, were used to achieve this objective.

1.2 Methods

1.2.1 Material

The alloy used in this work is part of the new family of Castable Nanostructured Alloys (CNAs), developed as part of the U.S.-led effort to further optimize RAFM steels for fusion applications by increasing MX precipitate number densities ($>10^{21\text{-}22}$ m^{-3}) with compositional modifications and thermomechanical treatments [4, 44-47]. This innovative approach has led to enhanced mechanical properties and radiation tolerance compared to preceding generations of FM and RAFM steels [1, 2, 4, 40, 44, 48-50]. The CNA steel used in this work is referred to as CNA9. It is a simple engineering analogue for more complex CNAs and was specifically developed to study the effects of carbon content on the microstructural evolution in CNAs. Through carbon content reduction and careful heat treatment design, CNA9 does not contain $M_{23}C_6$ precipitates. Hence, this low-carbon CNA steel was opted for this investigation over alternative CNA variants to isolate the irradiation effects on the MX precipitates and to avoid any influence from the $M_{23}C_6$ precipitates. CNA9 contains two TiC precipitate populations: small, elliptical MX-TiC precipitates with a diameter range of 3-18 nm (mean equivalent diameter = 7.9±0.3 nm) and large, spherical TiC precipitates with a diameter range of 50-100 nm. The small, elliptical MX-TiC precipitates are of interest in this work as they are hypothesized to be primary contributors to increased creep strength and radiation tolerance in the CNA variants.

The composition of CNA9 in weight percent is reported in Table 1. The bulk chemistry evaluation was performed by Dirats Laboratories using quantitative analysis by inductively

coupled plasma spectroscopy optical emission spectroscopy (ICP OES) for metallic elements, combustion for C and S, and inert gas fusion (IGF) for O and N. According to Dirats Laboratories, the uncertainty of each measurement was determined to be either 1% of the absolute composition value or two in the last reported digit, whichever is least. This method was used to determine the error of the analysis in Table 1.

CNA9 was normalized at 1050°C for 1 h in Ar atmosphere then hot-rolled at 1050°C to 0.3 inch-thick with ~21% reduction per pass. It was briefly reheated at 1050°C if needed followed by water quenching. The laboratory-scale ingot of CNA9 was then cut into two halves, top and bottom. The bottom half used in this work was tempered at 750°C for 30 min, air cooled, and de-scaled. A 1 cm piece from the top half was used for composition analysis [40]. Samples in the form of $1.5 \times 1.5 \times 10$ mm^3 bars were cut from the bottom half using electrical discharge machining (EDM) and polished with standard procedures, down to a final surface finish obtained using electropolishing. The electropolishing solution was 10% perchloric acid solution, 90% methanol solution, cooled to -45°C using a methanol bath with dry ice.

Table 1. Chemical compositions (wt%) of CNA9 provided by Dirats Laboratories.

Element	**CNA9 (wt.%)**
Fe	89.27±0.02
Cr	8.688±0.08688
W	1.026±0.0126
Mn	0.516±0.00516
Si	0.141±0.00141
Ta	0.090±0.0009
Ti	0.141±0.00141
V	0.049±0.00049
C	0.049±0.00049
Al	<0.002±0.0002

Journal Pre-proof

B	<0.0005±0.00005
Co	<0.005±0.0005
Cu	<0.002±0.0002
Mo	0.004±0.0004
Nb	<0.002±0.0004
Ni	<0.007±0.0007
P	0.004±0.0004
Zr	<0.002±0.0002
S	0.002±0.0002
O	0.0012±0.00012
N	0.0013±0.00013

Journal Pre-proof

1.2.2 Ion irradiation Experiments

The ex-situ ion irradiation experiments were conducted with 9 MeV Fe^{3+} ions at the University of Michigan-Ann Arbor's Michigan Ion Beam Laboratory (MIBL). The experiments tested the single and combined effects of temperature and damage level and will be discussed in three series: (1) a damage level series at constant temperature (1-10 0 dpa, 500°C), (2) a temperature series at constant intermediate damage level (15 dpa, 300-600°C), and (3) a temperature series at constant high damage level (50 dpa, 300 and 500°C) (Table 2, Figure 1). The

design of these irradiation series aimed to evaluate precipitate behavior under conditions relevant to fusion operation [28, 45], strategically spaced at damage level and temperature intervals conducive to conducting fundamental studies on precipitate behavior. The target matrix damage rate was 7×10^{-4} dpa/s, which is a commonly used dose rate for self-ion irradiation of FM and RAFM steels [46, 51]. Target matrix damage levels ranging from 1 to 100 dpa were used to gain a granular understanding of precipitate evolution. The target temperatures of 300, 400, 500, and 600ºC were used to encompass fusion-relevant temperatures and allow for a detailed understanding of operational mechanisms of precipitate stability as a function of thermal effects at the intermediate dose of 15 dpa. The elevated dose condition of 50 dpa at 300 and 500°C was used to ensure that temperature effects were not significant factors at elevated damage levels based on the initial findings found in the extended dose series component of this work.

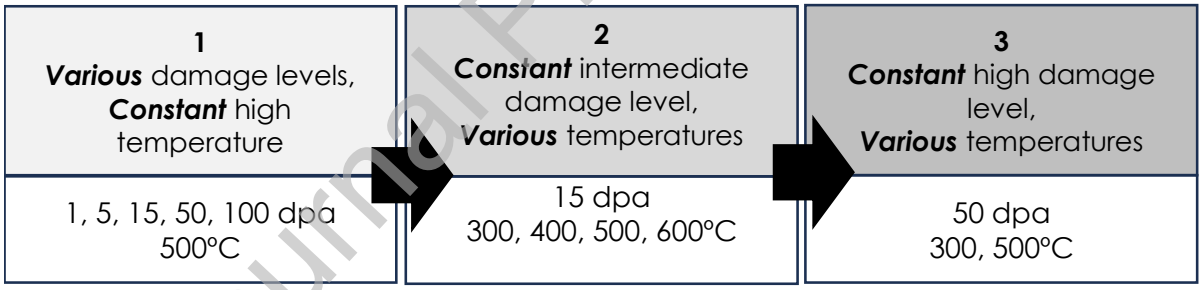

Figure 1 Graphical representation of the irradiation experiments conducted to understand the effects of irradiation on MX phase stability. All irradiations were conducted with a damage rate of 7×10^{-4} dpa/s.

Journal Pre-proof

Table 2 Ex-situ self-ion irradiation parameters. All irradiations were completed with 9 MeV Fe^{3+}. The cells are filled as follows: target parameter/achieved parameter experimentally. For simplicity, the target experimental parameters for each irradiation will be shown in the rest of this work. T_{irr} = temperature of irradiation.

T_{irr} (°C)	**Total dpa**	**Dose rate (dpa/s)**
300/298.2	15/15.1	$7\times10^{-4}/7\times10^{-4}$
300/294	50/50.4	$7\times10^{-4}/7\times10^{-4}$
400/399	15/15	$7\times10^{-4}/7.2\times10^{-4}$
500/503	1/1.1	$7\times10^{-4}/7.4\times10^{-4}$
500/502	5/5.3	$7\times10^{-4}/6.8\times10^{-4}$
500/500.6	15/15	$7\times10^{-4}/7.1\times10^{-4}$
500/499.8	50/50	$7\times10^{-4}/7.3\times10^{-4}$
500/499.6	100/100	$7\times10^{-4}/7.4\times10^{-4}$
600/601	15/15.4	$7\times10^{-4}/6.9\times10^{-4}$

The "quick" Kinchin-Pease (KP) mode in the Stopping and Range of Ions in Matter (SRIM 2013) [52] was used to calculate the depth-dependent damage in CNA9 from the 9 MeV Fe^{3+} ions [53, 54]. Figure 2 shows example damage profiles calculated for the 15 and 50 dpa irradiations and the nominal damage region used. The overall shape of the damage peak and the injected Fe ions is indicative of self-ion irradiations, where the near end of range exhibits a Gaussian peak based on the stochastic nature of the low-energy nuclear stopping of ions. The damage level induced in the CNA9 matrix shown in Figure 2 will be different than that in the MX-TiC precipitates due to the differences in composition and structure between the matrix and the precipitates. The damage level induced in the MX-TiC precipitates was also calculated to assess the evolution of precipitates with irradiation. The details of how this was calculated using SRIM can be found in Appendix A in the Supplemental. It was determined that the damage level in the MX-TiC precipitates was ~0.467× less than the level in the CNA9 matrix in the nominal damage region shown in Figure 2. The result is the following dose relationships between the matrix and the precipitates: $0.5_{TiC}/1_{matrix}$ dpa, $2.3_{TiC}/5_{matrix}$ dpa, $7_{TiC}/15_{matrix}$ dpa, $23_{TiC}/50_{matrix}$ dpa and $46_{TiC}/100_{matrix}$ dpa.

Temperature, pressure, beam current, and beam profiles were monitored during the irradiation experiments. Temperature was controlled to within ±10ºC of the target value during

experiments with the use of an infrared thermal pyrometer, thermocouple readings, and modulation of the back heater used within the stage design. The beam current was controlled to within ±10% of the desired current resulting in a damage rate of 7×10^{-4} dpa/s for all irradiations. All irradiations were completed with carbon contamination methods in place based on the recommendations within Was et al. [55].

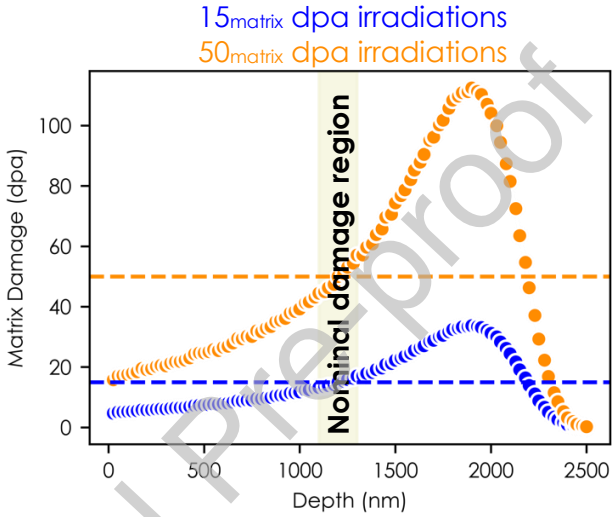

Figure 2 Calculated matrix damage profiles for the 15 (blue line) and 50 dpa (orange line) irradiations (ion direction is left-to-right of page). The target damage levels in the matrix were reached in the nominal damage region 1,100-1,300 nm beneath the surface.

1.2.3 Sample preparation and characterization

Conventional and scanning transmission electron microscopy (S/TEM) were used to identify and analyze the MX-TiC precipitates. A standard TEM sample preparation methodology created lift-outs for S/TEM analysis. Energy-filtered TEM (EFTEM)-based procedures [56] on a Thermo Fisher Tecnai G2 F30 TWIN Electron Microscope (TF30) equipped with a Gatan® Imaging Filter (GIF) were conducted on lift-outs to obtain the lift-out thicknesses. Multiple TEM liftouts were taken per sample and assessed. This ensured statistical significance and accounted for microstructural heterogeneity. The thickness of each liftout in the exact location where the

STEM-EDS maps were taken was assessed to obtain accurate density and volume fractions. The thickness of each liftout was kept between 80 and 130 nm. MX-TiC precipitates were identified through elemental mapping using STEM equipped with Energy Dispersive X-ray Spectroscopy (EDS) capability on the Thermo Fisher Talos F200X G2 S/TEM using the high-visibility low-background double-tilt ($\alpha = \pm 35°$, $\beta = \pm 30°$) holder for optimized EDS acquisition. Although STEM-EDS was used to identify the MX-TiC precipitates, precise quantitative compositional analysis of the MX precipitates was not performed due to their small size (<10 nm diameter) and embedment within the specimen volumes. Data acquisition was completed using Velox software. All microscopes used were part of the Michigan Center for Materials Characterization ($(MC)^2$) facility.

The average and standard error values of MX-TiC precipitate number density (ρ), equivalent diameter (d), and volume fraction (f) were calculated for each irradiation condition by assessing the MX-TiC precipitates in the STEM-EDS maps taken: the precipitates in each sample of a given thickness were counted to obtain ρ, the major (a) and minor (b) axes of each precipitate were measured to obtain the equivalent diameter ($d = \sqrt{a \times b}$), and the total volume of precipitates per condition was calculated to obtain volume fraction. The image processing software called FIJI, or ImageJ, was used for this analysis [57]. The standard errors reported represent the heterogeneity present in those variables. The Gaussian kernel density estimation with the built-in Python 3.7 Seaborn violin plot function [58] and built-in bandwidth Scott criterion [59] assessment was used to visualize the MX-TiC precipitate size distributions. The violin plots were scaled by width. Individual measurements of precipitate diameters were also overlaid onto the violin plots with symbols to illustrate the total precipitate number count for each condition studied.

1.3 Results and Discussion

1.3.1 As-received samples

The as-received (AR) sample was never thermally annealed after initial heat treatment or irradiated. An example STEM-EDS Ti map with the corresponding STEM-annular bright field (ABF) micrograph of the as-received condition of CNA9 are shown in Figure 3. Refer to Appendix B for a full analysis of the precipitates in the as-received sample. The mean number density of $(2.3\pm0.3)\times10^{21}$ m^{-3} MX-TiC precipitates in the as-received CNA9 sample is about 1-2 orders of magnitude greater than MX-(V,Nb)(C,N) precipitates found in Grade 91 steel, a second generation FM steel, and earlier generations of 9Cr RAFM steels [47, 49]. The MX precipitates in the as-received sample had an average equivalent diameter of 7.8±0.3 nm, a maximum diameter of 13.1 nm, and a minimum diameter of 3.3 nm.

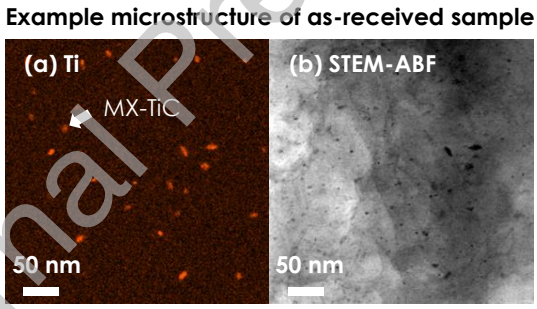

Figure 3 An example (a) STEM-EDS Ti map with the corresponding (b) STEM-ABF micrograph of the as-received sample.

1.3.2 Temperature series to $7_{TiC}/15_{matrix}$ dpa

The first irradiation series tested CNA9 samples at 300, 400, 500, and 600ºC to $7_{TiC}/15_{matrix}$ dpa. However, it is necessary to benchmark the MX-TiC precipitate behavior in samples subjected only to thermal annealing to differentiate the effects of thermal annealing from irradiation at these temperatures. An assessment of the precipitates subjected only to thermal annealing at 300, 400,

500, and 600ºC for ~6 hours, which is the time of the irradiation to $7_{TiC}/15_{matrix}$ dpa with 7×10^{-4} dpa/s, was conducted. Figure 4 shows the STEM-EDS Ti maps with the corresponding size distribution of precipitates for each annealing condition examined. These distributions are also compared to the as-received precipitate size distribution for reference. The dashed lines on the violin plots represent the 25% and 75% interquartile lines. Violin plots typically plot the median of the size distribution but here the mean values of the diameters for each condition are shown in between the 25% and 75% interquartile lines.

It was concluded that the precipitates remained thermally stable at the temperatures and time at temperatures tested as compared to the as-received condition. Accordingly, the evolution in precipitate statistics and size distributions will be ascertained by comparing the irradiated results to the results from the aggregated as-received and thermally annealed precipitate populations. This aggregated precipitate population is referred to as the control condition (CTRL) and is shown as the right-most size distribution in Figure 4. For the sake of clear visualization, the circular symbols representing individual counts of precipitates in the control condition will not be overlaid in subsequent figures, as the numerous counts obscure the shape of the violin plot.

Journal Pre-proof

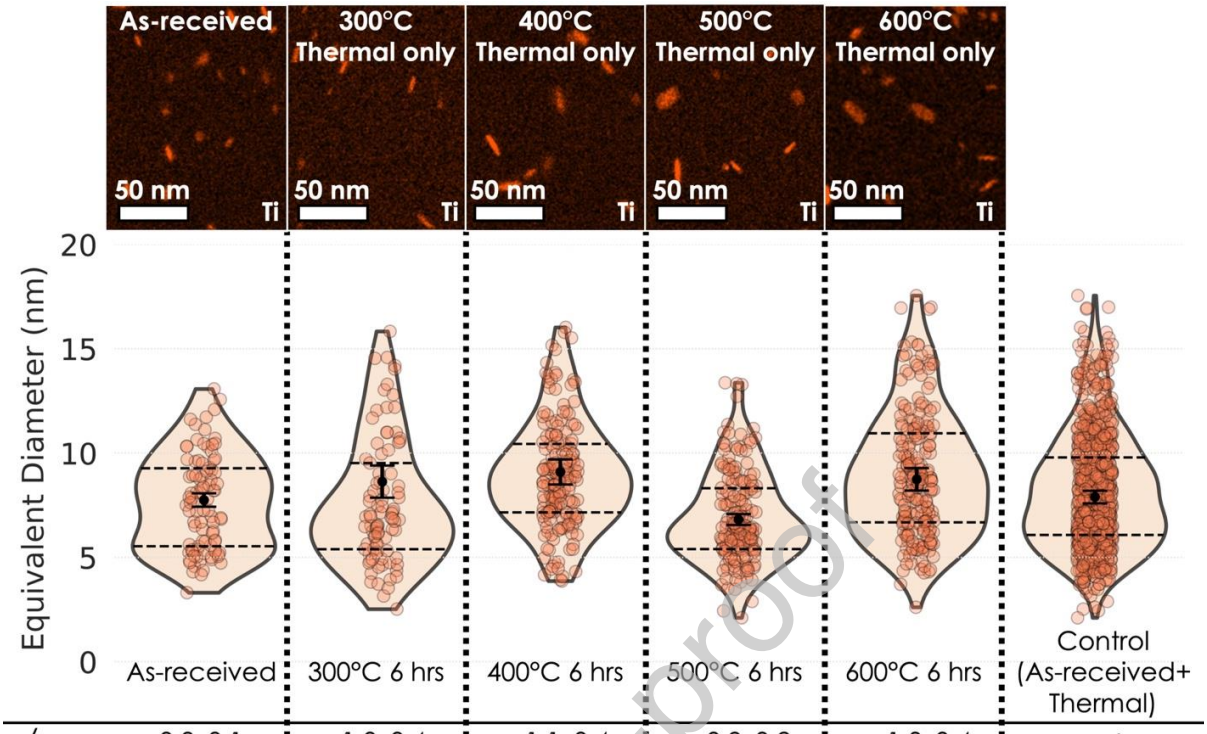

	As-received	300°C 6 hrs	400°C 6 hrs	500°C 6 hrs	600°C 6 hrs	Control (As-received+ Thermal)
ρ/ρ_{CTRL}	0.8±0.1	1.0±0.4	1.1±0.4	0.9±0.2	1.3±0.4	1
d/d_{CTRL}	1.0±0.1	1.1±0.1	1.2±0.1	0.9±0.1	1.1±0.1	1
f/f_{CTRL}	0.8±0.1	1.0±0.3	1.4±0.3	0.6±0.2	1.8±0.7	1

Figure 4 STEM-EDS micrographs with corresponding size distributions and precipitation statistics for the as-received specimen and the thermally annealed conditions at 300, 400, 500, and 600°C. The aggregated precipitate populations of the as-received and all thermally annealed conditions are shown via the distribution labeled 'Control.' Each condition was annealed for 6 hours. The dashed lines on the violin plots represent the 25% and 75% interquartile lines, in between which is the mean value of the diameter for that condition.

To further assess the inherent heterogeneity present in the CNA9 microstructure, the ratios of number densities (ρ/ρ_{CTRL}), equivalent diameters (d/d_{CTRL}), and volume fractions (f/f_{CTRL}) of the precipitates present in the as-received and in each thermally annealed condition were taken as a function of the control condition. This analysis is shown in the table beneath the precipitate size distributions in Figure 4. To determine the statistical significance of changes to precipitates caused by irradiation, the irradiated precipitate size distribution and statistics will be compared to the most conservative values of the ratios ρ/ρ_{CTRL}, d/d_{CTRL}, and f/f_{CTRL} tabulated in Figure 4. These conservative values are shown in Table 3 for reference.

Table 3 Tabulated values from Figure 4 that represent the range of statistical significance for ratio calculations between irradiated and control specimens.

Ratio	Significant if less than	Significant if greater than
ρ_{IRR}/ρ_{CTRL}	0.6	1.7
d_{IRR}/d_{CTRL}	0.8	1.3
f_{IRR}/f_{CTRL}	0.4	2.5

Now that the general statistics of the precipitates in the control condition have been formulated, the precipitates present in the samples irradiated to $7_{TiC}/15_{matrix}$ dpa can be analyzed. Figure 5 shows the STEM-EDS micrographs for each condition in the temperature series (300, 400, 500, and 600ºC) irradiated to $7_{TiC}/15_{matrix}$ dpa along with any changes present from the control size distribution of the MX-TiC precipitates based on the split violin plots where the right side contains the irradiation-induced size distribution. The statistical precipitate responses to irradiation as compared to the control condition are displayed below the size distribution plots (ρ_{IRR}/ρ_{CTRL}, d_{IRR}/d_{CTRL}, and f_{IRR}/f_{CTRL}), where bolded values in the figure mean that variable underwent a statistically significant change with irradiation (refer to Table 3). Refer to Appendix C in the Supplemental for all data on precipitate statistics in each irradiated condition (*i.e.*, number of EDS maps taken, number of precipitates counted, etc.).

The first noticeable effect of irradiation is the significant decrease in the number density of MX-TiC precipitates at low temperatures (300 and 400°C), as shown by the reported values for ρ_{IRR}/ρ_{CTRL}: **0.3±0.1** and **0.5±0.1**, respectively (Figure 5, Table 3). However, the average precipitate sizes remained stable after irradiation (d_{IRR}/d_{CTRL} = 1.1±0.1 and 1.0±0.1, respectively, for 300 and 400°C) as well as the 25% and 75% interquartile values. The resultant decreases in volume fractions are then primarily derived from the decreases in number densities (f_{IRR}/f_{CTRL} = **0.4±0.1** and 0.5±0.1, respectively).

It is necessary to address the observation in Figure 5 where the precipitate density decreases significantly at 300 and 400°C post-irradiation, yet the average precipitate size remains stable. This phenomenon likely results from the detection limits of the STEM-EDS technique. Precipitates smaller than ~2.5 nm, which is the assumed resolution cutoff (a few pixels), may fall below the detectable range, leading to an underestimation of the smallest precipitate populations and artificially stabilizing the size distribution. Additionally, irradiation may reduce the Ti content in precipitates due to ballistic ejection, decreasing the Ti signal of precipitates and complicating precipitate detection using STEM-EDS. If this is the case, the Ti may diffuse to other features in the microstructure, such as the larger TiC precipitates that do not dissolve, or to grain boundaries. A brief assessment of the solute segregation at all temperatures in Figure 5 was performed and no conclusive evidence of Ti segregation was found. The results suggest that ejected Ti was likely dissolved in the matrix under these conditions, but such minute changes in matrix composition are below the quantitative limit of the STEM-EDS technique deployed within. Therefore, the findings at 300°C and 400°C suggest dissolution, but it is recommended that future studies consider higher resolution techniques to better ascertain the evolution of size distributions within this temperature regime.

Journal Pre-proof

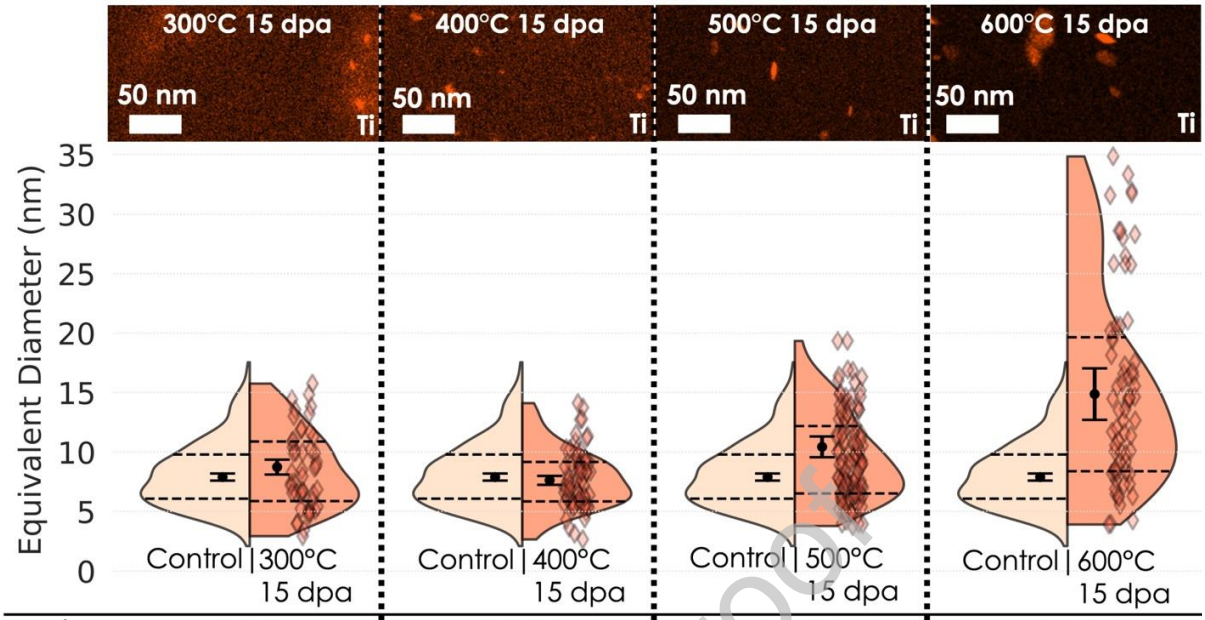

ρ_{IRR}/ρ_{CTRL}	**0.3±0.1**	**0.5±0.1**	**0.6±0.1**	**0.5±0.1**
d_{IRR}/d_{CTRL}	1.1±0.1	1.0±0.1	**1.3±0.1**	**1.9±0.3**
f_{IRR}/f_{CTRL}	**0.4±0.1**	0.5±0.1	1.2±0.3	**4.7±1.4**

Figure 5 STEM-EDS micrographs for the control specimen and each irradiated condition in the single beam temperature series irradiated to $7_{TiC}/15_{matrix}$ dpa, along with the corresponding split violin plots and the statistical precipitate responses to irradiation (ρ_{IRR}/ρ_{CTRL}, d_{IRR}/d_{CTRL}, and f_{IRR}/f_{CTRL}). Statistically significant changes in the precipitation response to irradiation are bolded. Symbols depicting individually measured precipitates are not shown overlaid on the control size distribution for clarity, refer to Figure 4 for such a representation.

The most noticeable effect of irradiation at elevated temperatures is the upward shifts in the tail of the size distributions at 500 and 600°C. This is reflected in the significant increases in average equivalent diameters (d_{IRR}/d_{CTRL} = **1.3±0.1** and **1.9±0.3**, respectively, for 500 and 600°C). The increases in precipitate sizes are most pronounced at 600°C, where the 25% interquartile line increased by ~45%, the mean increased by ~100%, the 75% interquartile line increased by ~110%, and the maximum increased by ~105% over the control condition. At 500°C, only the average size and the 75% interquartile line increased over the control condition. This difference may be due to the increased diffusion at 600°C causing greater levels of coarsening across the precipitate size spectrum. The number densities of precipitates also decreased significantly with irradiation at 500

and 600°C (**0.6±0.1** and **0.5±0.1**, respectively). As the volume fraction is most sensitive to changes in precipitate size ($f \sim r^3$), the volume fraction significantly increased at 600°C despite the decrease in number density (**4.7±1.4**).

In summary, at lower temperatures (300 and 400°C), ballistic dissolution appears to be the dominant process, resulting in partial dissolution of MX-TiC precipitates by $7_{TiC}/15_{matrix}$ dpa. These results are in line with previous literature that shows ballistic dissolution to be more dominant at lower temperatures [60]. However, the precipitate size behavior at 500 and 600°C may be consistent with radiation-enhanced coarsening [61, 62]. An analysis provided no conclusive evidence that Ostwald-ripening was the primary coarsening mechanism at 500°C (Appendix D in the Supplemental). Even if radiation-induced Ostwald ripening is not occurring or is merely one of the coarsening mechanisms occurring, diffusion-mediated coarsening appears to be operational on precipitate stability at 500 and 600°C as shown by the upward shifts of the precipitate size distributions and significant increases in the average equivalent diameters over the control condition.

1.3.3 Damage level series at 500°C

Based on the previous set of experiments, precipitate behavior at a temperature of 500°C irradiated to $0.5_{TiC}/1_{matrix}$, $2.3_{TiC}/5_{matrix}$, $7_{TiC}/15_{matrix}$, $23_{TiC}/50_{matrix}$, and $47_{TiC}/100_{matrix}$ dpa were chosen for further evaluation. The temperature of 500°C was chosen as it represents a shift in precipitate behavior from ballistic dissolution at lower temperatures to radiation-enhanced growth; noticeable coarsening took place at $7_{TiC}/15_{matrix}$ dpa and it is of interest to determine if this coarsening is a function of damage level; and 500°C is most likely closest to the peak swelling temperature of CNA9, which will be important for ascertaining precipitate behavior-swelling

relationships in future corresponding dual ion irradiations which were completed as a part of this series of works.

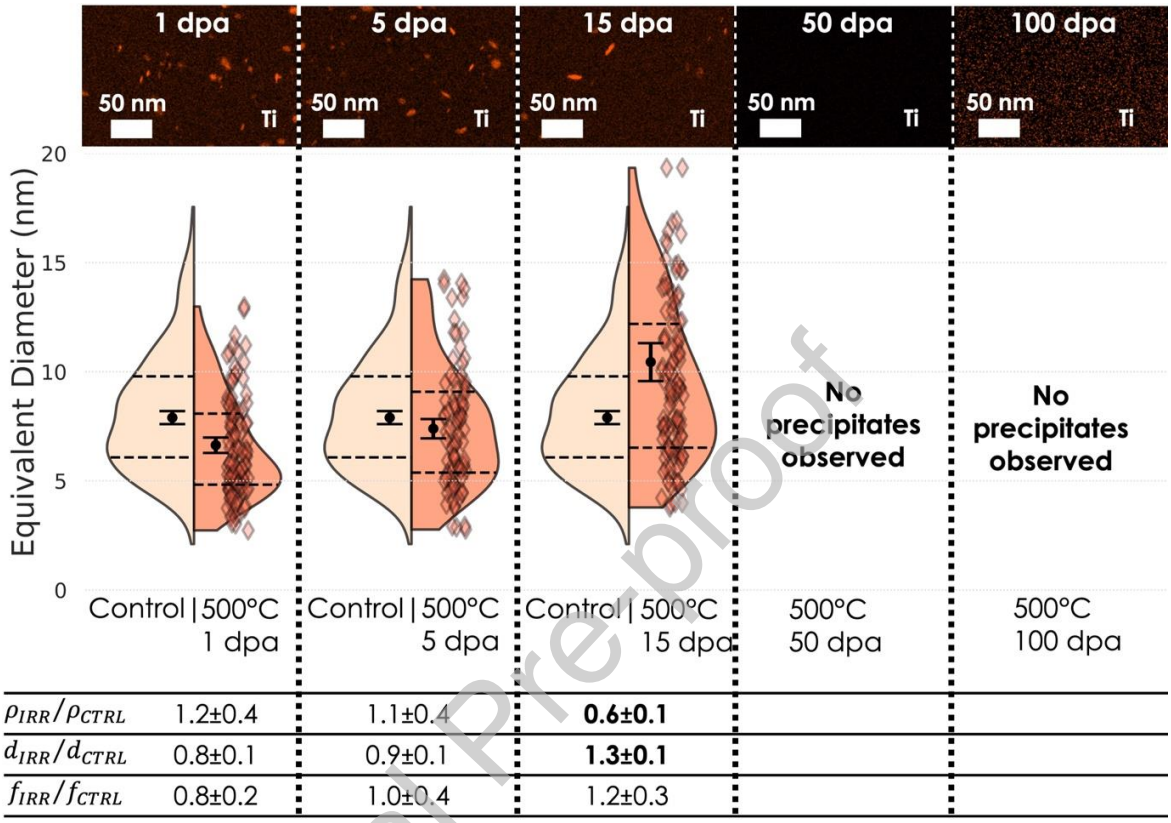

ρ_{IRR}/ρ_{CTRL}	1.2±0.4	1.1±0.4	**0.6±0.1**		
d_{IRR}/d_{CTRL}	0.8±0.1	0.9±0.1	**1.3±0.1**		
f_{IRR}/f_{CTRL}	0.8±0.2	1.0±0.4	1.2±0.3		

Figure 6 STEM-EDS micrographs of Ti with corresponding MX-TiC precipitate size distributions and statistics for the control specimen and specimens irradiated at 500°C to 1, 5, 15, 50, and 100 dpa_{matrix}. Individual measurements of precipitates are shown by markers overlaid on the violin plot size distributions.

Figure 6 highlights the significant impact of damage level on precipitate dissolution. The precipitates do not undergo statistically significant changes at low damage levels in density, size, or volume fraction – essentially, they are stable at and below 5 dpa_{matrix}. As discussed in the previous section, precipitates at 15 dpa_{matrix} displayed radiation-enhanced growth. However, the MX-TiC precipitates have completely dissolved at 50 dpa_{matrix} and 100 dpa_{matrix}. These experiments show that the mechanisms of precipitate behavior at 500°C is dependent on damage level – displaying an evolution of stability ($0.5_{TiC}/1_{matrix}$, $2.3_{TiC}/5_{matrix}$ dpa), growth ($7_{TiC}/15_{matrix}$

pa), and dissolution ($23_{TiC}/50_{matrix}$, $47_{TiC}/100_{matrix}$ dpa). It is assumed that the recoiled Ti atoms from the MX-TiC precipitates dissolve into the matrix.

1.3.4 Temperature series to $23_{TiC}/50_{matrix}$ dpa

The MX-TiC precipitates were shown to behave differently at low versus high temperatures at the intermediate damage level of $7_{TiC}/15_{matrix}$ dpa in previous sections. To further explore the temperature dependencies, two more irradiations at 300 and 500°C were conducted to high damage level. These temperatures were chosen because precipitates were shown to be in different regimes of stability at 300 and 500°C (partial dissolution and radiation-enhanced coarsening, respectively) at the intermediate damage level. Thus, this experimental series explores the evolution of those mechanisms at the elevated damage level of $23_{TiC}/50_{matrix}$ dpa.

Example STEM-EDS composition maps of Ti in Figure 8 display that the MX-TiC precipitates dissolved by $23_{TiC}/50_{matrix}$ dpa at both 300 and 500°C in the nominal irradiation region. It is possible that not all the MX-TiC precipitates dissolved in these conditions, but that the precipitate density was below detection due to the limited volume able to be assessed with the STEM-EDS technique or that the precipitate sizes were below the STEM-EDS probe resolution of ~0.5 nm. As no precipitates were present in the irradiated conditions, a detailed analysis of the precipitates in the thermally annealed conditions was not conducted. However, upon inspection of STEM-EDS maps taken of thermally annealed precipitates for these conditions, the precipitate sizes were visually in line with the control condition, though the number density appeared to decrease in the 500°C thermal condition (Appendix E in the Supplemental). MX-TiC precipitates display a high level of thermal stability in the literature as well [21, 33]. These experiments show that damage level is the dominant factor in precipitate dissolution by $23_{TiC}/50_{matrix}$ dpa for the temperatures (300, 500°C) and damage rate (7×10^{-4} dpa/s) studied.

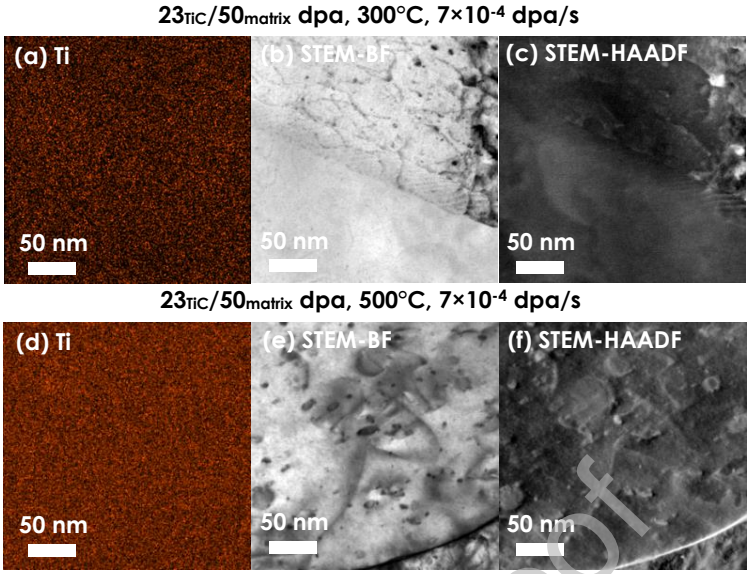

Figure 8 (a) STEM-EDS Ti map encompassing the nominal damage region with corresponding (b) STEM-BF and (c) STEM-HAADF maps for the sample irradiated to $23_{TiC}/50_{matrix}$ dpa at 300°C. (d) STEM-EDS Ti map encompassing the nominal damage region with corresponding (e) STEM-BF and (f) STEM-HAADF maps for the sample irradiated to $23_{TiC}/50_{matrix}$ dpa at 500°C.

1.3.5 Mathematical Model of MX-TiC Precipitate Stability

Thus far, the MX-TiC precipitates have been experimentally shown to display temperature-dominated responses at intermediate damage level ($7_{TiC}/15_{matrix}$ dpa) and damage-dominated responses by high damage level ($23_{TiC}/50_{matrix}$ dpa). To further explore the interrelationship between irradiation conditions and microstructural evolution, the modified version of the Nelson et al. (NHM model) by Zhao et al. was evaluated against the experimental data. Here, the modified variant by Zhao et al. will be referred to as the NHM-Z model and the modifications will be discussed after establishing the basis for the original NHM model. Unlike similar models like the Muroga, Kitajima, and Ishino (MKI) model [63] which only explores the explicit implications of ballistic dissolution, the NHM model simulates how a precipitate population under thermal or thermal and irradiation conditions can either grow, stay stable, or dissolve by the direct competition between recoil resolution and back diffusion of ejected solute. Recoil resolution is

also referred to as ballistic dissolution in literature, where collision cascades during irradiation cause the ballistic ejection of solute atoms from precipitates into the matrix [60]. The base NHM model is given as,

$$\frac{dr}{dt} = -\frac{f_m G}{N_{at}} + \frac{3D^{irr} \times \frac{4}{3}\pi n r^3 p + c}{4} - D^{irr} n r^2 \qquad \text{Eqn. 1}$$

where f_m is a multiplication factor that accounts for the recoil resolution rate with units of atoms/cm^2×dpa, G is the dose rate in dpa/s, N_{at} is the atomic density of the matrix, D^{irr} is the diffusion coefficient which under irradiation is the radiation enhanced diffusion coefficient, p is the atomic fraction of solute in the precipitate, c is the atomic fraction of solute in the matrix, n is the number density of precipitates and r is the radius of the precipitate. In this case the first term and third term in Eqn. 1 leads to precipitate dissolution while the second term leads to diffusion-driven growth. The original work using Eq. 1 was applied to both dissolution of Ni-Al during ion bombardments and $M_{23}C_6$ carbides in alloy PE16 [64] and more recently applied to a range of clustering and precipitate phenomena in Fe-based alloys [65]. Importantly, the NMH model has been used in literature to ascertain a critical balance in the dissolution rate and growth rate at various irradiation temperatures within these material systems.

Several modifications of the NHM model have been proposed including those by Frost and Russell [66] as well in the work by Zhao et al. The Frost and Russell work considered additional physical mechanisms, most importantly the solute deposition rate is a function of the proximity to the precipitate while the modifications by Zhao et al. are refinements based on more modern conceptualizations of point defect formation via displacements and cascades as well as improvements based on the fundamental derivations. Specifically, the NMH-Z modifications to the original NMH model are four-fold. First the model accounts for the post-cascade quench point

defect production efficiency in the matrix by integrating a vacancy production efficiency term with common literature values for self-ion irradiations being at or between 0.1 and 0.2 [67, 68]. Second, the matrix solute concentration is modified to be the solute supersaturation level by subtracting the thermal solubility limit, c_{eq}, from the calculation. Third, the precipitate growth rate term is rederived within their work showing a prefactor of 4π. Finally, the boundary condition of constant solute concentration within the material is modified to account for high (>5%) phase fractions by subtracting the solute concentration in the precipitates. Additional details on the modifications, including detailed derivations, are provided within Zhou et al. [69].

The resulting mathematical NHM-Z model then renders the following equation to calculate the change in precipitate radius with irradiation:

$$\frac{dr}{dt} = -\frac{f_m G}{N_{at}} + \frac{D^{irr} C}{rp} \times \frac{3}{3 - 4\pi n r^3} - \frac{D^{irr}}{rp} \times \left(\frac{4\pi n r^3 p}{3 - 4\pi n r^3} + c_{eq} \right) \qquad \text{Eqn. 2}$$

Where C is given by:

$$C = p \times \frac{4}{3}\pi r^3 n + c \times \left(1 - \frac{4}{3}\pi r^3 n\right), \qquad \text{Eqn. 3}$$

and, the calculation proposed by Marwick et al. for f_m is used:

$$f_m = \frac{1}{6} \frac{p - c_{eq}}{a_n} (d_n a_n)^2 \qquad \text{Eqn. 4}$$

where a_n is the nearest neighbor distance and d_n is a modifier to indicate the capture radius of a precipitate undergoing irradiation. In this work, d_n is a simple integer to facilitate parameter searches, but later iterations could include a more scientifically informed calculations for $d_n a_n$ such as via rigorous atomistic simulations which fall outside of the scope of the current work. Zhao

et al. showed the modifications to provide reasonable approximations of experimentally observed α′ precipitate radii in irradiated Cr-rich Fe alloys where α′ precipitate radiation stability is known to be sensitive to irradiation conditions including temperature, dose rate, and cascade type [60, 70, 71].

Both Eqns. 1 and 2, require the determination of radiation enhanced diffusion coefficient, D^{irr}. A full description of the calculations for D^{irr} using standard rate theory calculations and the microscopic diffusion parameters are provided in Appendix F of the Supplemental. Key in the calculations for D^{irr} is the migration energy for vacancies and interstitials as well as the determination of the irradiation-enhanced concentrations of vacancies and interstitials which is dependent on the total sink strength and recombination rate for interstitials and vacancies. The microscopic diffusion parameters in Fe-Cr alloys have been well studied, but there exists limited literature on the Fe-Ti system [38, 65, 72-75].

To parameterize the NMH-Z model for the Fe-Ti system under consideration for MX TiC precipitates a two-step search procedure using Python was used. This script searched for optimized inputs based on the presented experimental precipitate stability data under both irradiation and only thermal exposure at 15 dpa (Figure 5), minor coarsening under thermal only conditions at 50 dpa at 500°C (Figure 6) and known dissolution at 50 dpa at 500°C (Figure 6) and assumed instability of precipitates at 300°C and 400°C at 50 dpa. A pseudo-code description of the full procedure and outputs is provided in Appendix G of the Supplemental Material. In short, the first step defined relevant ranges for input parameters into Eqn. 2 and D^{irr} and 1000 iterations to 15 dpa were run randomly selecting values within the defined input ranges. From these 1000 iterations, the simulated mean diameter ratio, $\left(D_{ppt}^{irr-15dpa,sim} / D_{ppt}^{CTRL}\right)$, is calculated and the mean average error (MAE) is calculated against the experimentally determined irradiation-induced and

thermally-induced ratios provided in Figure 5. The 50-input variable sets that define the microscopic diffusion with the lowest MAE are then set as fixed inputs and the second step is conducted. This effectively locks in the thermal diffusion parameters. In the second step, the model is reparametrized for only the starting number density and size of precipitates while also integrating relevant ranges for dislocation loop size and density based on ranges derived from literature values. Another 1000 model iterations are run to 50 dpa with the MAE calculated assuming complete dissolution of precipitates. The parameterized variable set and corresponding values for precipitate diameters under irradiation that has the lowest combined MAE between the first and second runs are used to evaluate the NHM-Z model.

To more accurately represent the evolution of the entire precipitate population under irradiation using the NHM-Z, each iteration performed assumed an initial Gaussian population of 200 individual precipitates that are scaled to the input total density and sized based on the experimental population were individually simulated using Eqn. 2 and the mean diameter values extracted at each dose increment based on this population. A special condition was set that any precipitate that fell below 1 nm in size was removed from the population, assuming these are not experimentally detectable using the STEM-EDS conditions used within.

The found model parameters are provided in Table 4 and Table 5 while the predicted MX TiC precipitate diameter ratios based on the calculated diffusion coefficients are compared to the experimental values in Figure 9. Note, the values for the composition inputs were varied with temperature based on Thermo-Calc simulations to accurately reflect the solubility variation in Ti with varying sample temperature. Additionally, in this study, the characterization of the dislocation loops was limited due to the primary and demanding focus of capturing MX-TiC precipitates experimentally. Consequently, the values for dislocation loop size and density in Table 5 are

predictions rather than direct measurements. Despite this limitation, the model was structured to optimize its loop size and density selection within defined bounds for each temperature range. The optimization results presented in Table 5 align well with established trends in the literature regarding dislocation loop evolution in FM and RAFM steels. Specifically, the increase in dislocation loop size with temperature is consistent with previous studies using the same ion irradiation facilities and controls as those within this work. For example, the recent work by Clowers et al. which under similar dual-ion irradiations at 50 dpa with 10 appm He co-injection in F82H showed an increase in dislocation loop size from 10 nm to 20 nm between 400 to 500°C and a corresponding decrease in loop density at 500°C with no observable loops above 500°C [76]. It should be noted that helium implantation levels have been shown to impact the dislocation structure by altering the ratio of dislocation loop types in FM steels, but not the number density of total dislocation loops [77]. The ranges provided in Table 5 for dislocation loops are also consistent with values for HT9 [78] and Grade 91 [47, 79] irradiated using single Fe-ions. Furthermore, the observed decrease in loop density from 500°C to 400°C corresponds to the known behavior where higher temperatures produce larger but less dense loops [9, 80].

While the values used in Table 5 for dislocation loop evolution are based on predictive modeling and not cross-verified with literature values from experimental measurements for dislocation loops, they nevertheless provide a degree of confidence. The necessity of smaller, high-density loops at lower temperatures and larger, low-density loops at 500°C was observed across all model iterations during the optimization steps. In addition, each model's iteration required loop sizes of the same scale (10s of nm) and the same order of magnitude in density for each temperature. This strongly suggests that dislocation loop evolution is critical towards the model response, as will be discussed later, and that the dislocation loop evolution must be consistent with

established literature trends. Given this, it is acknowledged that the values used in Table 5 should be cautiously considered due to their lack of full experimental parameterization.

Table 4 Variables and their values used in the diffusion calculations.

Variable	Symbol	Value
Jump frequency [81]	α	Vacancies: 1.6×10^{13} Hz Interstitials: 2.9×10^{12} Hz
Lattice parameter of the matrix	a	2.96 Å
Interstitial formation entropy	S_f^v	2.17 ev/K
Vacancy formation entropy	S_m^i	0 eV/K
Interstitial formation energy	E_f^v	1.5 eV
Vacancy formation energy	E_f^i	3.5 eV
Interstitial migration energy	E_m^v	0.93 eV
Vacancy migration energy	E_m^i	0.35 eV

Table 5 Variables and their values used in the NHM-Z calculations.

Variable	Symbol	Value
Defect production efficiency	ζ	0.25
Solute displacement distance	d_n	4
Combinatorial factor	z_{iv}	50
Dislocation Loop Diameter / Density at 300°C	$\rho_L^{300°C}$	15 dpa: 0 50 dpa: 9.75 nm / 4.9×10^{22} m^{-3}
Dislocation Loop Diameter / Density at 400°C	$\rho_L^{400°C}$	15 dpa: 0 50 dpa: 13.75 nm / 8.6×10^{22} m^{-2}
Dislocation Loop Diameter / Density at 500°C	$\rho_L^{500°C}$	15 dpa: 0 50 dpa: 39.00 nm / 8.1×10^{21} m^{-2}
Dislocation Loop Diameter / Density at 600°C	$\rho_L^{600°C}$	15 dpa: 0 50 dpa: 0
Line Dislocation Density	ρ_t	2×10^{14} m^{-2}
Prior austenite grain diameter	d_{PAG}	12 µm
Equivalent lath diameter	d_{Lath}	20 nm
Dislocation bias [82]	$z_{i,v}$	Vacancies: 1.00 Interstitials: 1.08

The NHM-Z model predicts the overall evolution of the MX-TiC precipitates, where at temperatures below 600°C, the thermal diffusion of Ti is sufficiently low that thermal or irradiation-enhanced coarsening does not occur up to $7_{TiC}/15_{matrix}$ dpa in the given sink-strength conditions. The radiation-enhanced diffusion coefficients in Figure 9b shows that the increased coarsening in the $7_{TiC}/15_{matrix}$ dpa irradiation condition at 600°C is due to the increased point defect concentration of vacancies and interstitials induced by irradiation which drives the D^{irr} to higher

Journal Pre-proof

values than D^{th}. This response for radiation-enhanced coarsening was also observed experimentally for 600°C at 15 dpa in Figure 5. At lower temperatures, it was found based on the model that recombination becomes more dominant, and the thermally induced concentration of vacancies is sufficiently low that D^{irr} is suppressed to levels where there is insufficient time under irradiation or thermal exposure only to impose coarsening. In Figure 9a, the 300°C condition overestimates the ballistic dissolution, indicating further refinement of the input parameters for the NHM-Z model are needed, or additional mechanisms not considered within the model are impacting the observed experimental stability at lower temperatures (300°C).

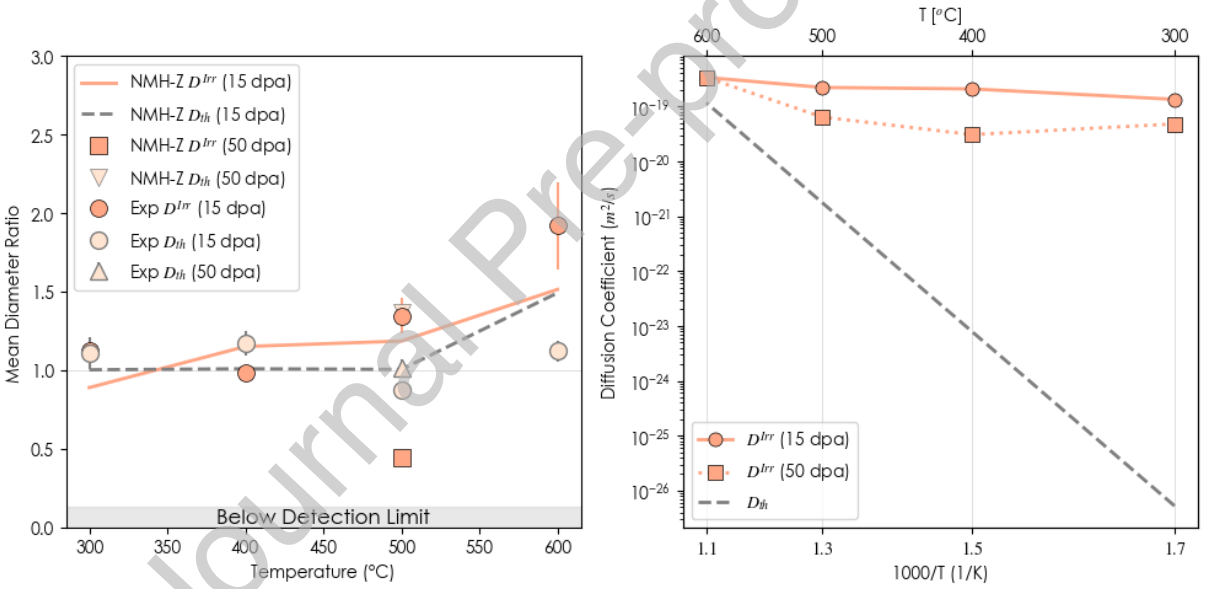

Figure 9 Plots showing (a) the theoretical behavior of MX-TiC precipitates under irradiation to $7_{TiC}/15_{matrix}$ dpa and $23_{TiC}/50_{matrix}$ dpa as modelled by the NHM-Z model and (b) the calculated change in the radiation-enhanced diffusion coefficient due to increase total sink strength contributions based predicted dislocation loop evolution.

The NMH-Z also helps highlight the balance between back diffusion and recoil resolution under the evolving conditions based the $7_{TiC}/15_{matrix}$ dpa condition. Extensive work on other ferritic/martensitic steels under neutron and ion irradiation conditions have shown dislocation loops evolution with loop densities between effectively zero due to detection limits and ~8×10^{21}

m^{-3} and loop sizes ranging from 0 to ~40 nm under similar irradiation conditions [9, 80]. These loops act as additional point defect sinks which in turn would suppress the overall radiation-enhanced diffusion based on the underlying rate theory calculations where increased sink strengths drive lower point defect concentrations. As seen in Figure 9a, when dislocation loop evolution is considered for the $23_{TiC}/50_{matrix}$ condition, the model predicts precipitate dissolution with the predicted mean diameter ratio for the MX-TiC precipitates approaching the experimental observability limit. The inversion from stability to instability between the $7_{TiC}/15_{matrix}$ dpa and the $23_{TiC}/50_{matrix}$ conditions based on the model is due to the dislocation loop evolution increasing the effective sink strength with increasing irradiation dose. The increased sink strength at the higher dose reduces the total concentration of point defects that lowers the effective Ti diffusion for the same irradiation temperature conditions as observed in Figure 9b. The NHM-Z model suggests that the dominant influence on the precipitate behavior switches from back diffusion mediated stability at intermediate damage levels to dissolution-induced instability at high damage level based on the dynamic evolution of co-existing defect sinks present in the irradiated CNA materials.

The analysis and conclusion that microstructural evolution of other features, such as dislocation loops, can upset the precipitate behavior based on the NHM-Z model is consistent with similar observations in other material systems. For example, previous research on MX-TiC precipitates in austenitic Ti-modified stainless steel concluded that the dissolution of MX-TiC precipitates between 10 and 45 dpa corresponded to the formation of other secondary phases, such as phosphides and the G phase [37]. These secondary phases acted as additional sinks, reducing the overall effective diffusion coefficient while also trapping Ti atoms redistributed to MX precipitates leading to their dissolution. Though the radiation-induced nucleation of new Ti-containing phases was not explicitly observed for CNA9, it is possible that Ti atoms redistributed

to other features (i.e., to the larger, stable TiC precipitates or to grain boundaries) during irradiation which impacted the TiC solubility limit. Such a driving force for redistribution would have caused the diffusion of Ti atoms away from the MX-TiC precipitates, effectively causing reducing their size to zero.

1.3.6 Constraints and Limitations Affecting MX-TiC Precipitate Stability Analysis

The mathematical model applied within simplifies a highly complex physical system by assuming an average homogeneous behavior across the precipitate population. However, it's important to acknowledge that the MX-TiC precipitates exhibit significant heterogeneity, as demonstrated in the Supplemental Information through detailed analysis of various STEM-EDS as-received maps. While the model offers valuable insights into general trends as shown in Figure 9, it does not capture the localized and atomistic phenomena that may be critical in the real system. Previous works suggest that closely spaced precipitates could potentially exchange solute atoms under irradiation, enhancing overall precipitate stability [83, 84]. Despite our efforts, we found no experimental evidence of such solute exchange under the studied conditions, though the possibility of localized effects remains.

Furthermore, the applied model does not account for the impact of interfacial energy related to the precipitate-matrix interface's dislocation structure. The as-received precipitates are characterized as semi-coherent with the matrix, as detailed in Appendix H. The strain field around a precipitate—and consequently, the near-interface point defect diffusivity—is significantly influenced by the interfacial dislocation structure [85, 86]. It has been shown that as damage levels increase, these interfacial dislocation structures may become unstable, potentially leading to changes in precipitate size or even dissolution [87-89].

Journal Pre-proof

Thus, at higher damage levels, the possible diminishing strains around the MX precipitates and potential loss of interfacial dislocation structures may affect solute replenishment or alter the precipitate defect bias, contributing to dissolution. This mechanism could operate alongside the dynamic evolution of other microstructural sinks, such as dislocation loops, and thus could be highly difficult to deconvolute both experimentally using conventional techniques deployed within and with the simplifying assumptions that form the basis of the NMH-Z model.

The NMH-Z model's other limitations include its omission of morphological and compositional evolution impacts, which could alter interfacial characteristics like energy, misfitting dislocation structures, lattice strains, and other factors. These changes might influence precipitate coarsening rates, solute recoil distances, interparticle spacing, binding interactions within precipitates, the presence of other phases, and solute solubility limits under irradiation.

Addressing these model shortcomings necessitates recognizing the inherent complexities and the circular logic arising from parameterizing the model with our experimental findings. While the model aligns well with established literature mechanisms for precipitate stability, these complexities indicate that a more thorough exploration is needed. Given the physical intricacies and the challenges associated with high-fidelity experiments, it is suggested that comprehensive multi-scale modeling, including extensive atomistic modeling, is crucial to advance our understanding of precipitate stability in complex irradiation environments. Such studies should incorporate actual atomic-level structures and interface properties of the MX-TiC particles and the surrounding matrix. This step is vital for fully understanding MX-TiC stability and developing a robust predictive model for alloy design and material properties. However, this constitutes a substantial additional effort beyond the already extensive work presented herein.

Journal Pre-proof

Finally, it is crucial to highlight that our findings are derived from accelerated single-ion irradiations, and direct application to phase stability in a prototypic fusion energy system may be misleading due to additional complexities like transmutation products, which are not considered here. The follow-up paper will specifically address these aspects. Even with further studies, the dose rate disparity between this research and fusion power generation remains significant. This underscores the necessity of dedicating significant experimental effort toward dose-rate studies to enable more robust benchmarking of predictive models.

A summary of the overall findings from this work are presented in Table 6. The overall findings and supporting application of the NHM-Z model support observations in a wide-range of other materials systems – precipitate stability under irradiation is a balance between solute back diffusion and recoil resolution. Given this, the summary results in Table 6 are not fully aligned with other observations of other precipitates in RAFM steels [9, 10, 12-26, 28, 29]. For example, MX-(Ti,W,Ta)C precipitates in CNA3 were stable under irradiation to 50 dpa at 650°C (damage rate was not reported) [24]. Conversely, at lower temperatures, dissolution was observed by 50 dpa at 450°C and 50°C of the same alloy at a damage rate of 1×10^{-3} dpa/s, and dissolution of TaN, TaC, and VN was also observed at 500°C at ~5×10^{-4} dpa/s at 500°C [23] a result consistent with the recent work of Haley et al. that showed dissolution of VN throughout a 40-100 dpa damage layer in an advanced UKAEA developed steel [90]. The varying responses observed in literature compared to this systematic study highlight the overall complexity in precipitate of stability under both ion and neutron irradiations.

The assessment of which dominating factors at play for both Table 6 and the complex literature results remain mostly qualitative due to the existing limitations with experimental observation of dynamic behavior and the lack of a robust and flexible modelling framework for

complex, engineering-grade alloys such as CNA9. Ultimately, this field of research is ripe for developing quantitative understandings of precipitate evolution based on the listed interfacial characteristics, ultimately allowing for predictive capabilities in the MX-precipitate stability in advanced steels for fusion energy systems. Additionally, the ion irradiation experiments did not concurrently test the effects of creep, stress, and fatigue, which will be important for understanding how precipitates will respond under load during fusion plant operation. Lastly, there remains the open question of transmutation effects, of which helium co-injection during self-ion irradiation can be used to assess this precipitate behavior. As helium is expected to be an important microstructural modifier under fusion operation [91], such research is needed. This is the topic of the next effort in this series of work by the authors.

Table 6 Summary of the precipitate behavior in various temperature and damage level regimes from the experimental and MKI modeling results.

Damage Level Regime	**Temperature Regime**	**Suggested dominant mechanism affecting r_{cap}**	**Precipitate behavior**
Intermediate ($7_{TiC}/15_{matrix}$ dpa)	Low temperature (300, 400°C)	Low diffusion of Ti causing less solute migration back to precipitates	No size changes, but partial dissolution
	High temperature (500, 600°C)	High diffusion of Ti causing more solute migration to precipitates	Precipitate growth
High ($23_{TiC}/50_{matrix}$ dpa)	All temperatures (300, 500°C)	Ti solute redistribution, decreased diffusion due to increased sinks, and high interparticle spacing	Complete dissolution

1.4 Conclusion

In conclusion, an advanced Fe-9Cr RAFM, CNA9, was self-ion irradiated to ascertain the effects of temperature and damage level on MX-TiC precipitate stability:

- At intermediate damage levels ($7_{TiC}/15_{matrix}$ dpa), MX-TiC precipitates experienced dissolution at lower temperatures (300, 400°C) due to dominant ballistic effects. In

comparison, higher temperatures (500, 600°C) favored coarsening driven by radiation-enhanced diffusion, underscoring different stability mechanisms.

- The MX-TiC precipitate response was temperature-insensitive at higher damage levels ($23_{TiC}/50_{matrix}$ dpa and $47_{TiC}/100_{matrix}$ dpa). The MX precipitates fully dissolved at all temperatures tested at these higher damage levels (300, 500°C).
- The NHM-Z model was applied to rationalize the experimental observations, highlighting the interplay between recoil resolution and solute back diffusion. The model suggests that dynamic changes in defect sinks, particularly dislocation loops and the precipitates themselves, transition the system from a diffusion-dominated growth phase at lower doses to a dissolution-dominated stage at higher doses.
- Despite its utility in modeling precipitate behavior, the NHM-Z model falls short in considering the nuanced roles of morphological evolution and localized solute-exchange processes, leaving room for significant studies into these impacts to further refine current irradiation precipitate theories including the NHM-Z model used within.
- Due to their dissolution by $23_{TiC}/50_{matrix}$ dpa, any potential advantages in terms of mechanical properties or resistance to radiation damage provided by these precipitates could be lost in the early stages of fusion power plant operation, although the accelerated nature of the current study must be accounted for.

The effect of helium co-implantation on precipitate behavior will be assessed in the next report of this series by the authors.

Declaration of competing interest

Journal Pre-proof

The authors declare that they have no known competing financial interests or personal relationships that could have appeared to influence the work reported in this paper.

Acknowledgements

The experimental work presented here was funded by the Fusion Energy Sciences program (DOE-FOA-0002173). The authors also acknowledge the University of Michigan-Ann Arbor College of Engineering for financial support and the Michigan Center for Materials Characterization for use of the instruments and staff assistance. Research presented here was also partially supported by the Laboratory Directed Research and Development program of Los Alamos National Laboratory under project number XXPV. This research was partly sponsored by the US Department of Energy, Office of Fusion Energy Sciences under contract DE-AC05-00OR22725 with UT-Battelle, LLC.

References

1. H. Tanigawa, et al., *Development of benchmark reduced activation ferritic/martensitic steels for fusion energy applications.* Nuclear Fusion, 2017. **57**(092004).
2. S. J. Zinkle, et al., *Development of next generation tempered and ODS reduced activation ferritic/martensitic steels for fusion energy applications.* Nuclear Fusion, 2017. **57**(9).
3. S. Sojak, et al., *Bubble Swelling in Ferritic/Martensitic Steels Exposed to Radiation Environment with High Production Rate of Helium.* Materials, 2021. **14**(11).
4. L. Tan, Y. Katoh, and L.L. Snead, *Development of castable nanostructured alloys as a new generation RAFM steels.* Journal of Nuclear Materials, 2018. **511**: p. 598–604.
5. F. Abe, *Precipitate design for creep strengthening of 9% Cr tempered martensitic steel for ultra-supercritical power plants.* Sci Technol Adv Mater, 2008. **9**(1): p. 013002.
6. L.K. Mansur, et al., *Control of helium effects in irradiated materials based on theory and experiment.* Journal of Nuclear Materials, 1986. **141-143**: p. 633–646.
7. P.J. Maziasz, *Formation and stability of radiation-induced phases in neutron-irradiated austenitic and ferritic steels.* Journal of Nuclear Materials, 1989. **169**: p. 95–115.
8. A.F. Rowcliffe and E.H. Lee, *High temperature radiation damage phenomenon in complex alloys.* Journal of Nuclear Materials, 1982. **108 & 109**: p. 306–318.

9. C. Dethloff, E. Gaganidze, and J. Aktaa, *Microstructural defects in EUROFER 97 after different neutron irradiation conditions.* Nuclear Materials and Energy, 2016. **9**: p. 471–475.
10. C. Dethloff, E. Gaganidze, and J. Aktaa, *Quantitative TEM analysis of precipitation and grain boundary segregation in neutron irradiated EUROFER 97.* Journal of Nuclear Materials, 2014. **454**(1-3): p. 323–331.
11. A. Bhattacharya, et al., *Radiation induced amorphization of carbides in additively manufactured and conventional ferritic-martensitic steels: In-situ experiments on extraction replicas.* Journal of Nuclear Materials, 2022. **563**.
12. H. Yan, et al., *Phase stability and microstructural evolution in neutron-irradiated ferritic-martensitic steel HT9.* Journal of Nuclear Materials, 2021. **557**.
13. L. Tan, Y. Katoh, and L.L. Snead, *Stability of the strengthening nanoprecipitates in reduced activation ferritic steels under Fe2+ ion irradiation.* Journal of Nuclear Materials, 2014. **445**(1-3): p. 104–110.
14. P.J. Maziasz, R.L. Klueh, and J.M. Vitek, *Helium effects on void formation in 9Cr-1MoVNb and 12Cr-1MoVW Irradiated in HFIR.* Journal of Nuclear Materials, 1986. **141-143**: p. 929–937.
15. M. Tamura, et al., *Creep deformation of iron strengthened by MX type particles.* Journal of Nuclear Materials, 2004. **329-333**: p. 328–332.
16. B.H. Sencer, et al., *Microstructural evolution in modified 9Cr–1Mo ferriticmartensitic steel irradiated with mixed high-energy proton and neutron spectra at low temperatures.* Journal of Nuclear Materials, 2002. **307-311**: p. 266–271.
17. H. Tanigawa, et al., *Radiation induced phase instability of precipitates in reduced-activation ferritic/martensitic steels.* Journal of Nuclear Materials, 2007. **367-370**: p. 132–136.
18. H. Abe, et al., *Mechanism of instability of carbides in Fe–TaC alloy under high energy electron irradiation at 673 K.* Journal of Nuclear Materials, 2014. **455**(1-3): p. 695–699.
19. H. Abe, et al., *New Approach to in Situ Observation Experiments under Irradiation in High Voltage Electron Microscopes.* Materials Transactions, 2014. **55**(3): p. 423–427.
20. S. Kano, et al., *Instability of MX and M23C6 type precipitates in F82H steels under 2.8 MeV Fe2+ irradiation at 673 K.* Nuclear Materials and Energy, 2018. **17**: p. 56–61.
21. L. Tan, et al., *Stability of MX-type strengthening nanoprecipitates in ferritic steels under thermal aging, stress and ion irradiation.* Acta Materialia, 2014. **71**: p. 11–19.
22. *Fusion Materials Semiannual Progress Report for the Period ending December 31, 2020*. DOE-ER-0313/69, ORNL/SPR-2021/1910.
23. L. N. Clowers, Z. Jiao, and G.S. Was, *Synergies between H, He and radiation damage in dual and triple ion irradiation of candidate fusion blanket materials.* Journal of Nuclear Materials, 2022. **565**.
24. C.M. Parish, et al., *Helium sequestration at nanoparticle-matrix interfaces in helium + heavy ion irradiated nanostructured ferritic alloys.* Journal of Nuclear Materials, 2017. **483**: p. 21–34.
25. Z. Yan and Y. Lin, *The effect of sink strength on helium bubble formation at elevated temperatures.* Nuclear Analysis, 2022. **1**(1).
26. Y. Lin, et al., *Dynamic observation of dual-beam irradiated Fe and Fe-10Cr alloys at 435 °C.* Acta Materialia, 2021. **209**.

27. S.J. Zinkle, et al., *Multimodal options for materials research to advance the basis for fusion energy in the ITER era.* Nuclear Fusion, 2013. **53**(10).
28. S. J. Zinkle and J.T. Busby, *Structural materials for fission & fusion energy.* Materials Today, 2009. **12**(11).
29. G. S. Was, et al., *Materials for future nuclear energy systems.* Journal of Nuclear Materials, 2019. **527**.
30. E. H. Lee, A. F. Rowcliffe, and L.K. Mansur, *Precipitation and cavity formation in austenitic stainless steels during irradiation.* Joumal of Nuclear Materials, 1981. **103 & 104**: p. 1475–1480.
31. L. K. Mansur, *Theoretical evaluation of a mechanism of precipitate-enhanced cavity swelling during irradiation.* Philosophical Magazine A, 1981. **44**(4): p. 867–877.
32. L.K. Mansur and W.A. Coghlan, *Mechanisms of helium interaction with radiation effects in metals and alloys: A review.* Journal of Nuclear Materials, 1983. **119**: p. 1–25.
33. W. Kesternich, *Helium trapping at dislocations, precipitates and grain boundaries*, in *Radiation Effects*. 1983. p. 261–273.
34. W. Kesternich, *Dislocation-controlled precipitation of TiC particles and their resistance to coarsening.* Philosophical Magazine A, 1985. **52**(4): p. 533–548.
35. E.H. Lee, N.H. Packan, and L.K. Mansur, *Effects of pulsed dual-ion irradiation on phase transformations and microstructure in Ti-modified austenitic alloy.* Journal of Nuclear Materials, 1983. **117**: p. 123–133.
36. K. Farrell, et al., *Modification of radiation damage microstructure by helium.* Radiation Effects, 2006. **78**(1-4): p. 277–295.
37. T. Kimoto and H. Shiraishi, *Void swelling and precipitation in a titanium-modified austenitic stainless steel under proton irradiation.* Journal of Nuclear Materials, 1985. **132**: p. 266–276.
38. P.J. Maziasz, *Helium trapping at Ti-rich MC particles in Ti-modified austenitic stainless steel*. 1980, CONF–801072–10, ORNL.
39. L. Cui, et al., *APT characterization of irradiation effects on MX phase in reduced-activation ferritic/martensitic steels.* Journal of Nuclear Materials, 2023. **573**.
40. L. Tan, et al., *Recent status and improvement of reduced-activation ferritic-martensitic steels for high-temperature service.* Journal of Nuclear Materials, 2016. **479**: p. 515–523.
41. *Fusion Materials Semiannual Progress Report for the Period Ending June 30, 2021*. DOE-ER-0313/70, ORNL/SPR-2021/2151.
42. *Fusion Materials Semiannual Progress Report ending December 31, 2021*. DOE-ER-0313/71, ORNL/SPR-2022/2416.
43. *Fusion Materials Semiannual Progress Report for the Period ending December 31 2022*. DOE/ER-0313/73, ORNL/TM-2023/2934.
44. L. Tan, C. M. Parish, and X. Hu, *Microstructure and property tailoring of castable nanostructured alloys through thermomechanical treatments.* Journal of Nuclear Materials, 2018. **509**: p. 267–275.
45. L. K. Mansur, et al., *Materials needs for fusion, Generation IV fission reactors and spallation neutron sources – similarities and differences.* Journal of Nuclear Materials, 2004. **329-333**: p. 166–172.
46. S. Taller, et al., *Predicting structural material degradation in advanced nuclear reactors with ion irradiation.* Sci Rep, 2021. **11**(1): p. 2949.

Journal Pre-proof

47. G. S. Was, et al., *Emulation of reactor irradiation damage using ion beams.* Scripta Materialia, 2014. **88**: p. 33–36.
48. L. Tan, *Development of Nanoprecipitates- Strengthened Advanced Ferritic Alloys for Nuclear Reactor Applications*. 2019.
49. L. Tan, *Report on the Down-Selected Nanoprecipitates-Strengthened Advanced Ferritic Alloys for Nuclear Reactor Applications*. 2019.
50. L. Tan, *Mechanical Properties and Radiation Resistance of Nanoprecipitates-Strengthened Advanced Ferritic Alloys*. 2017.
51. P. Xiu, *Effects of Sink Strength and Irradiation Parameters on Defect Evolution in Additively Manufactured HT9*, in *Nuclear Engineering and Radiological Sciences*. 2022, University of Michigan, Doctoral Thesis.
52. J. F. Ziegler, M. D. Ziegler, and J.P. Biersack, *SRIM – The stopping and range of ions in matter (2010).* Nuclear Instruments and Methods in Physics Research Section B: Beam Interactions with Materials and Atoms, 2010. **268**(11-12): p. 1818–1823.
53. R. E. Stoller, et al., *On the use of SRIM for computing radiation damage exposure*. Nuclear Instruments and Methods in Physics Research Section B: Beam Interactions with Materials and Atoms, 2013. **310**: p. 75–80.
54. K. Nordlund, et al., *Improving atomic displacement and replacement calculations with physically realistic damage models.* Nat Commun, 2018. **9**(1): p. 1084.
55. G.S. Was, et al., *Resolution of the carbon contamination problem in ion irradiation experiments.* Nuclear Instruments and Methods in Physics Research Section B: Beam Interactions with Materials and Atoms, 2017. **412**: p. 58–65.
56. J. Bentley, *Energy-Filtered Imaging: A Tutorial.* Microscopy and Microanalysis, 2020. **6**(S2): p. 1186–1187.
57. C. A. Schneider, W .S. Rasband, and K.W. Eliceiri, *NIH Image to ImageJ: 25 years of image analysis.* Nat Methods, 2012. **9**(7): p. 671–5.
58. M. Waskom, *seaborn: statistical data visualization.* Journal of Open Source Software, 2021. **6**(60).
59. M. C. Jones, J. S. Marron, and S.J. Sheather, *A Brief Survey of Bandwidth Selection for Density Estimation.* Journal of the American Statistical Association, 1996. **91**(433): p. 401–407.
60. K. N. Thomas and G.S. Was, *Effect of cascade size and damage rate on α' precipitate stability in Fe-15Cr.* Journal of Nuclear Materials, 2023. **585**.
61. J. Ribis, *Phase Stability in Irradiated Alloys*, in *Comprehensive Nuclear Materials*. 2020. p. 265–309.
62. A. Baldan, *Progress in Ostwald ripening theories and their applications to the γ-precipitates in nickel-base superalloys.* Journal of Materials Science, 2002. **37**: p. 2379–2405.
63. T. E. Oliphant, *Python for Scientific Computing.* Computing in Science & Engineering, 2007. **9**(3): p. 10–20.
64. R. S. Nelson, J. A. Hudson, and D.J. Mazey, *The stability of precipitates in an irradiation environment.* Journal of Nuclear Materials, 1972. **44**: p. 318–330.
65. M. J. Swenson and J.P. Wharry, *Rate Theory Model of Irradiation-Induced Solute Clustering in b.c.c. Fe-Based Alloys.* Jom, 2020. **72**(11): p. 4017–4027.
66. H.J. Frost and K.C. Russell, *Particle stability with recoil resolution.* Acta Metallurgica, 1982. **30**: p. 953–960.

67. S.J. Zinkle and B.N. Singh, *Analysis of displacement damage and defect production under cascade damage conditions.* Journal of Nuclear Materials, 1993. **199**: p. 173–191.
68. K. Nordlund, et al., *Primary radiation damage: A review of current understanding and models.* Journal of Nuclear Materials, 2018. **512**: p. 450–479.
69. Y. Zhao, et al., *Effect of heavy ion irradiation dose rate and temperature on α′ precipitation in high purity Fe-18%Cr alloy.* Acta Materialia, 2022. **231**.
70. M. Bachhav, G. R. Odette, and E.A. Marquis, *α′ precipitation in neutron-irradiated Fe–Cr alloys.* Scripta Materialia, 2014. **74**: p. 48–51.
71. E. R. Reese, et al., *Dose rate dependence of Cr precipitation in an ion-irradiated Fe 18Cr alloy.* Scripta Materialia, 2018. **146**: p. 213–217.
72. J. Ding, et al., *Energetics of helium-vacancy complexes in Fe-9Cr alloys from first-principles calculations.* Journal of Nuclear Materials, 2019. **513**: p. 143–151.
73. K. C. Pitike, et al., *Helium interaction with solutes and impurities in neutron-irradiated nanostructured ferritic alloys: A first principles study.* Journal of Nuclear Materials, 2022. **566**.
74. D. Murali, et al., *Diffusion of Y and Ti/Zr in bcc iron: A first principles study.* Journal of Nuclear Materials, 2011. **419**(1-3): p. 208–212.
75. A. Salmasi, et al., *Mobilities of Ti and Fe in disordered TiFe-BCC assessed from new experimental data.* Calphad, 2021. **74**.
76. L.N. Clowers and G.S. Was, *The effect of hydrogen co-injection on the microstructure of triple ion irradiated F82H.* Journal of Nuclear Materials, 2024. **601**.
77. A. Bhattacharya, et al., *Helium causing disappearance of a/2<111> dislocation loops in binary Fe-Cr ferritic alloys.* Journal of Nuclear Materials, 2021. **556**.
78. D. Woodley, et al., *The Role of Co-injected Helium on Swelling and Cavity Evolution at High Damage Levels in Ferritic-Martensitic Steels.* Journal of Nuclear Materials, 2021. **550**.
79. S. Taller and G.S. Was, *Understanding bubble and void nucleation in dual ion irradiated T91 steel using single parameter experiments.* Acta Materialia, 2020. **198**: p. 47–60.
80. S. Taller, *The Role of Damage Rate on Cavity Nucleation with Co-Injected Helium in Dual Ion Irradiated T91 Steel*, in *Nuclear Engineering*. 2020, University of Michigan.
81. G. S. Was, *Fundamentals of Radiation Materials Science: Metals and Alloys*. 2nd ed. 2017: Springer.
82. A. A. Kohnert, M. A. Cusentino, and B.D. Wirth, *Molecular statics calculations of the biases and point defect capture volumes of small cavities.* Journal of Nuclear Materials, 2018. **499**: p. 480–489.
83. M. L. Lescoat, et al., *In situ TEM study of the stability of nano-oxides in ODS steels under ion-irradiation.* Journal of Nuclear Materials, 2012. **428**(1-3): p. 176–182.
84. K.C. Russell, *Phase instability under cascade damage irradiation.* Journal of Nuclear Materials, 1993. **206**: p. 129–138.
85. M. Mock, et al., *Modeling the influence of strain fields around precipitates on defect equilibria and kinetics under irradiation in ODS steels: A multi scale approach.* Journal of Nuclear Materials, 2019. **527**(151807).
86. A. Vattre, et al., *Non-random walk diffusion enhances the sink strength of semicoherent interfaces.* Nat Commun, 2016. **7**: p. 10424.

87. T. Chen, et al., *Temperature dependent dispersoid stability in ion-irradiated ferritic-martensitic dual-phase oxide-dispersion-strengthened alloy: Coherent interfaces vs. incoherent interfaces.* Acta Materialia, 2016. **116**: p. 29–42.
88. L. Wang, et al., *Effect of sink strength on coherency loss of precipitates in dilute Cu-base alloys during in situ ion irradiation.* Acta Materialia, 2021. **210**.
89. W.V. Vaidya, *Modification of the precipitate interface under irradiation and its effect on the stability of precipitates.* Journal of Nuclear Materials, 1979. **83**: p. 223–230.
90. Haley, J., et al., *Short communication: Complete dissolution of MX-phase nanoprecipitates in fusion steels during irradiation by heavy-ions.* Journal of Nuclear Materials, 2024. **596**.
91. H. Ullmaier, *The influence of helium on the bulk properties of fusion reactor structural materials.* Nuclear Fusion, 1984. **24**(8): p. 1039–1083.

Graphical Abstract

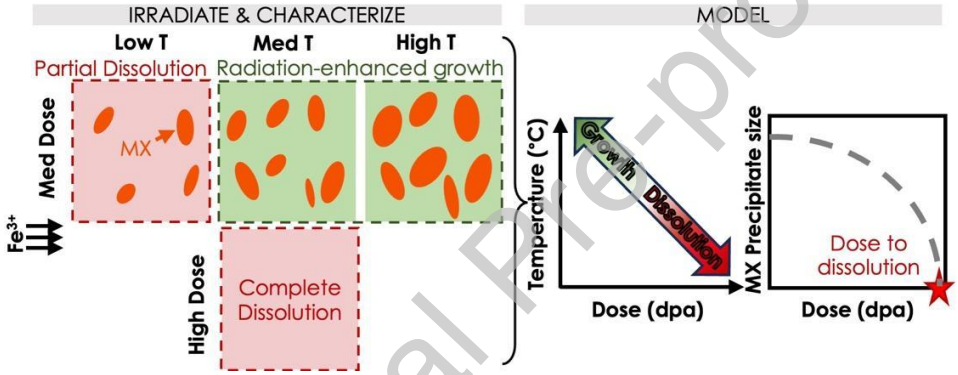

Declaration of interests

☒ The authors declare that they have no known competing financial interests or personal relationships that could have appeared to influence the work reported in this paper.

Journal Pre-proof